Gas tunnel engineering of prolyl hydroxylase reprograms hypoxia signaling in cells

Peter Windsor[¶], Haiping Ouyang[§], Joseph A. G. da Costa[¶], Anoop Rama Damodaran[¶]*, Yue Chen[§]*, Ambika Bhagi-Damodaran[¶]*

[¶]Department of Chemistry, [§]Department of Biochemistry and Molecular Biology, University of Minnesota, Twin Cities, Minneapolis, MN-55455, USA.

*Corresponding author emails: rdanoop@umn.edu, yuechen@umn.edu, ambikab@umn.edu

Abstract

Molecular engineering of biocatalysts has revolutionized complex synthetic chemistry and sustainable catalysis. Here, we show that it is also possible to use engineered biocatalysts to reprogram signal transduction in human cells. More specifically, we manipulate cellular hypoxia (low O_2) signaling by engineering the gas-delivery tunnel of prolyl hydroxylase 2 (PHD2), an iron-dependent enzymatic O_2 sensor. Using computational modeling and rational protein design techniques, we resolve PHD2's gas tunnel and critical residues therein that limit the flow of O_2 to PHD2's catalytic core. Systematic modification of these residues open the constriction topology of PHD2's gas tunnel with the most effectively designed mutant displaying 11-fold enhanced hydroxylation efficiency. Furthermore, transfection of plasmids that express these engineered PHD2 mutants in HEK-293T cells reveal significant reduction in the levels of hypoxia inducible factor (HIF-1α) even under hypoxic conditions. Our studies reveal that activated PHD2 mutants can reprogram downstream HIF pathways in cells to simulate physiological O_2-like conditions despite extreme hypoxia and underscores the potential of engineered biocatalysts in controlling cellular function.

Introduction

From oxygen reduction during respiration to ammonia synthesis during nitrogen fixation, iron enzymes enable numerous physiological processes. Consequently, iron enzymes in their wild type (WT) or engineered forms are being increasingly utilized for sustainable synthesis of complex

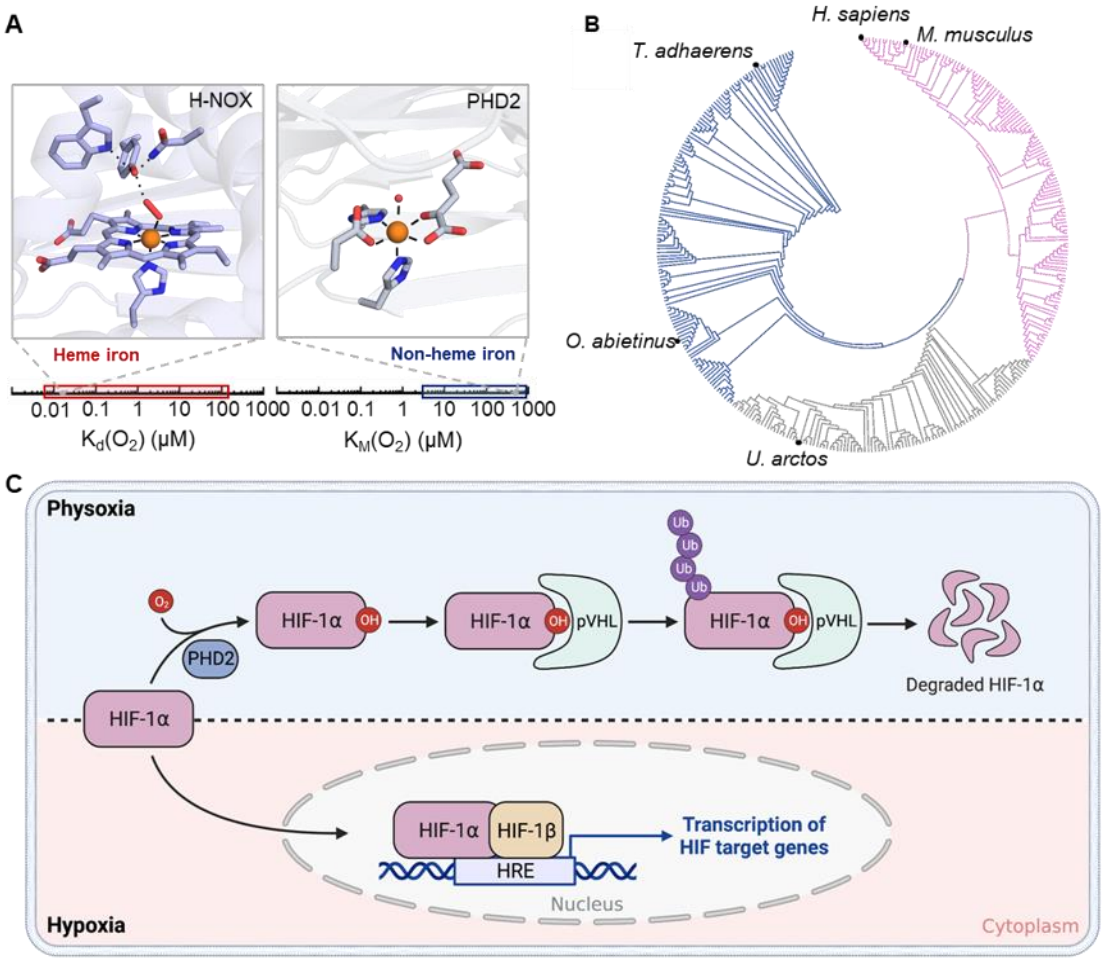

Figure 1: Iron-dependent biocatalysts are widely utilized for hypoxia signaling in cells A) Left panel shows the primary and secondary coordination sphere of a heme iron-dependent O_2 sensing protein, H-NOX (PDB: 3EEE). O_2 is stabilized in the structure by a hydrogen-bond triad. Right panel shows the primary coordination sphere of a non-heme iron-dependent O_2 sensing protein, PHD2 (PDB: 5L9B). The scales below the structures show ranges of O_2 K_d values (red) of heme iron-based sensors and the O_2 K_M values (blue) of non-heme iron-based sensors. **B)** Protein phylogeny of PHD2 (EGLN1) across 1844 organisms. PHD2s are well conserved throughout evolution with the protein being observed in simple animals such as *T. adhaerens* up to complex mammals such as *H. sapiens.* **C)** A simplistic cartoon representation of HIF-based hypoxia signal transduction in mammalian cells. Under adequate O_2 levels (physoxia), PHD2 catalyzes hydroxylation of HIF-1α leading to its subsequent proteosomal degradation. Under hypoxia, however, PHD2 is limited by co-substrate O_2 levels leading to HIF-1α accumulation. HIF-1α, thereby, translocates to the nucleus where it upregulates transcription of 70 hypoxia response gene elements (HRE) to restore O_2 homeostasis.

chemicals and natural products[1] as well as to run biofuel cells.[2] Iron containing proteins also facilitate sensing and signaling of oxygen (O_2), a critical metabolite required for oxidative phosphorylation and energy generation in cells. Different cell types utilize either heme and non-heme iron proteins to recognize, respond and adapt to change in O_2 levels.[3-4] Heme-based sensors bind O_2 directly to the iron center with affinities that range widely from low nanomolar to high micromolar concentrations (left panel, **Fig. 1A** and **Table S1**).[5,6,7] As an example, *C.*

subterraneous H-NOX utilizes its distorted porphyrin macrocycle and extensive hydrogen-bonding network to bind O_2 with a high affinity and low dissociation constant ($K_{d(O2)}$) of 23 nM.[8,5] Non-heme iron-based sensors, on the other hand, utilize O_2 as a co-substrate to catalyze a hydroxylation reaction.[9] A prime example of a non-heme iron-based O_2 sensor is mammalian prolyl hydroxylase 2 (PHD2/ELGN1) that utilizes O_2 to catalyze hydroxylation of hypoxia-inducible transcription factor (HIF-1α) (right panel, **Fig. 1A**).[10,11] The sensing capability of PHD2-like non-heme iron-based enzymatic O_2 sensors is often discussed in terms of their Michaelis constant ($K_{M(O2)}$), and varies widely from low micromolar to a millimolar (**Table S2**).[6] Unlike heme-based O_2 sensors, however, the structural and molecular features that govern the sensing capability of non-heme iron-based O_2 sensors are relatively unexplored.[12,13] This gap in knowledge remains despite the prevalence of non-heme iron-based enzymatic O_2 sensors in bacteria, single-celled eukaryotes, and animals.[6,14,15]

Iron in PHD2 is coordinated to a 2-oxoglutarate (2OG) cofactor, two histidines and an aspartate from the protein (right panel, **Fig. 1A**).[16] Upon binding HIF-1α transcription factor, iron reacts with O_2 to form a high-valent ferryl species that enables HIF-1α hydroxylation.[17] Phylogenetic analysis of PHD2 suggests that the protein is highly conserved across the animal kingdom, from simple organisms like *Trichoplax adhaerens* to more complex ones like *Homo sapiens* (**Fig. 1B**).[15,18] These homologs exhibit >84% primary sequence conservation in their N-terminus zinc finger domain (21-58) and C-terminus hydroxylase domain (181-426) (**Fig. S1**). The zinc finger domain has been shown to be important in the recruitment of PHD2 to hydroxylate HIF-1α in *H. sapiens*.[19] Specifically, mammalian cells utilize PHD2 to differentiate between hypoxia (low O_2; $[O_2]$<3%) and physiological O_2 conditions or physoxia (5% O_2).[20,21] Under physoxia (region shaded blue in **Fig. 1C**), PHD2 utilizes co-substrate O_2 to hydroxylate two proline residues in the N-terminal and C-terminal O_2-dependent degradation domains (NODD and CODD) of HIF-1α.[22,23] Hydroxylation of one or both of these proline residues creates a binding site for the Von Hippel Lindau protein (pVHL) which leads to polyubiquitination and subsequent

degradation by the E3 ligase complex.[24,25] Under hypoxia (region shaded pink in **Fig. 1C**), hydroxylation of HIF-1α by PHD2 is O_2-limited leading to its accumulation in the cytosol.[11] Cytosolic HIF-1α translocates to the nucleus and forms a transcription complex with HIF1-β (ARNT) and p300.[26] The ternary complex then binds to hypoxia response gene elements (HRE) to initiate the transcription of 70 genes that modulate physiology via changes in metabolism, angiogenesis, and erythropoiesis to allow for hypoxia adaptation and O_2 homeostasis restoration.[27,28,9] These hypoxia activated genes show significant upregulation in several disease types such as cancer and Alzheimer's.[29,30,31,32] Consequently, the HIF-signaling pathway has emerged as a prominent therapeutic target for the treatment of these diseases.

Previous studies have reported the $K_{M(O2)}$ of PHD2 to lie in the 400-600 μM range,[6,33] which is much higher than analogues enzymes (**Table S2**). PHD2's $K_{M(O2)}$ is tuned to such high values so the enzyme can differentiate between physoxia and hypoxia. A recent multiscale computational study has highlighted presence of a single unusually narrow hydrophobic gas tunnel for O_2 to access the iron center in PHD2.[34] In this study, we use structure-guided computational modeling and protein design approaches to further investigate the structural and molecular basis of O_2 sensing by PHD2. More specifically, we identify several critical residues lining the gas tunnel of PHD2 that limit the flow of O_2 to PHD2's catalytic iron core. We show that rational and systematic modification of these gas tunnel residues can open the constriction topology of PHD2's gas tunnel and reduce the $K_{M(O2)}$ value from 415±36 μM for WT PHD2 to 161±17 μM for the most effectively designed mutant. This mutant involves the substitution of two bulky tryptophan residues in PHD2's gas tunnel to smaller phenylalanine residues and demonstrates 11-fold enhancement in hydroxylation efficiency in an enzymatic assay employing a peptide-based HIF-1α mimic. Furthermore, transfection of plasmids that express these designed PHD2 variants reduce HIF-1α levels in HEK-293T cells by two-fold. Overall, this study brings forth the use of engineered and activated PHD2 as a novel mechanism to manipulate hypoxia signaling in cells as well as answers longstanding questions in bioinorganic chemistry and chemical biology by providing insights into

the molecular and structural basis of O_2 sensitivities of iron-based enzymatic sensors. From a biocatalysis perspective, this work showcases the potential of using engineered enzymes to modulate signaling pathways and cellular function.

Results and Discussion

We note that the iron atom in PHD2 is buried in the protein's macromolecular structure such that a tunnel would be required for O_2 gas to reach the iron core. Such O_2-delivering tunnels have also been structurally and biochemically characterized for various heme-based O_2 transporting proteins and gas sensors, such as H-NOX and myoglobin.[35,36] To better resolve O_2 transport tunnels connecting the catalytic iron center to the surface of PHD2, we used CAVER[37] – a software tool that visualizes and analyzes tunnels and channels in protein structures. We used the crystal structure of PHD2 complexed with CODD peptide (PDB: 5L9B) for these analyses since PHD2 is known to bind O_2 only after its association with CODD or NODD domains of HIF-1α.[38,39] The CAVER program identified a single narrow tunnel created by the interface between PHD2 and CODD (**Fig. 2A**). The tunnel is mainly comprised of PHD2 residues with bulky non-polar characteristics (I256, W258, M299, I327, and W389) along with some polar residues (Q239, R252, and T387) (**Fig. 2B**). Three residues (P564, Y565 and I566 colored teal, **Fig. 2B**) from the CODD substrate (HIF-1α mimic) also contributed to forming the tunnel. A select set of these residues have been previously identified to contribute to the rate of O_2 entry to PHD2's active site.[34] The predominant non-polar nature of this tunnel aligns with its function as the path for non-polar O_2 gas. Our analysis of CODD-bound PHD2 crystal structure identified a bottleneck (labeled BN, **Fig. 2B**) in the gas tunnel that was mainly formed by residues M299 and W389 in PHD2 and P564 in CODD. We hypothesized that the presence of large amino acid residues like Met, Trp, Ile, and Arg in PHD2's gas tunnel could restrict O_2 transport to PHD2's active site which may ultimately determine its O_2 sensing capability and hydroxylation activity. To investigate this possibility, we undertook a computation- and structure-guided rational design

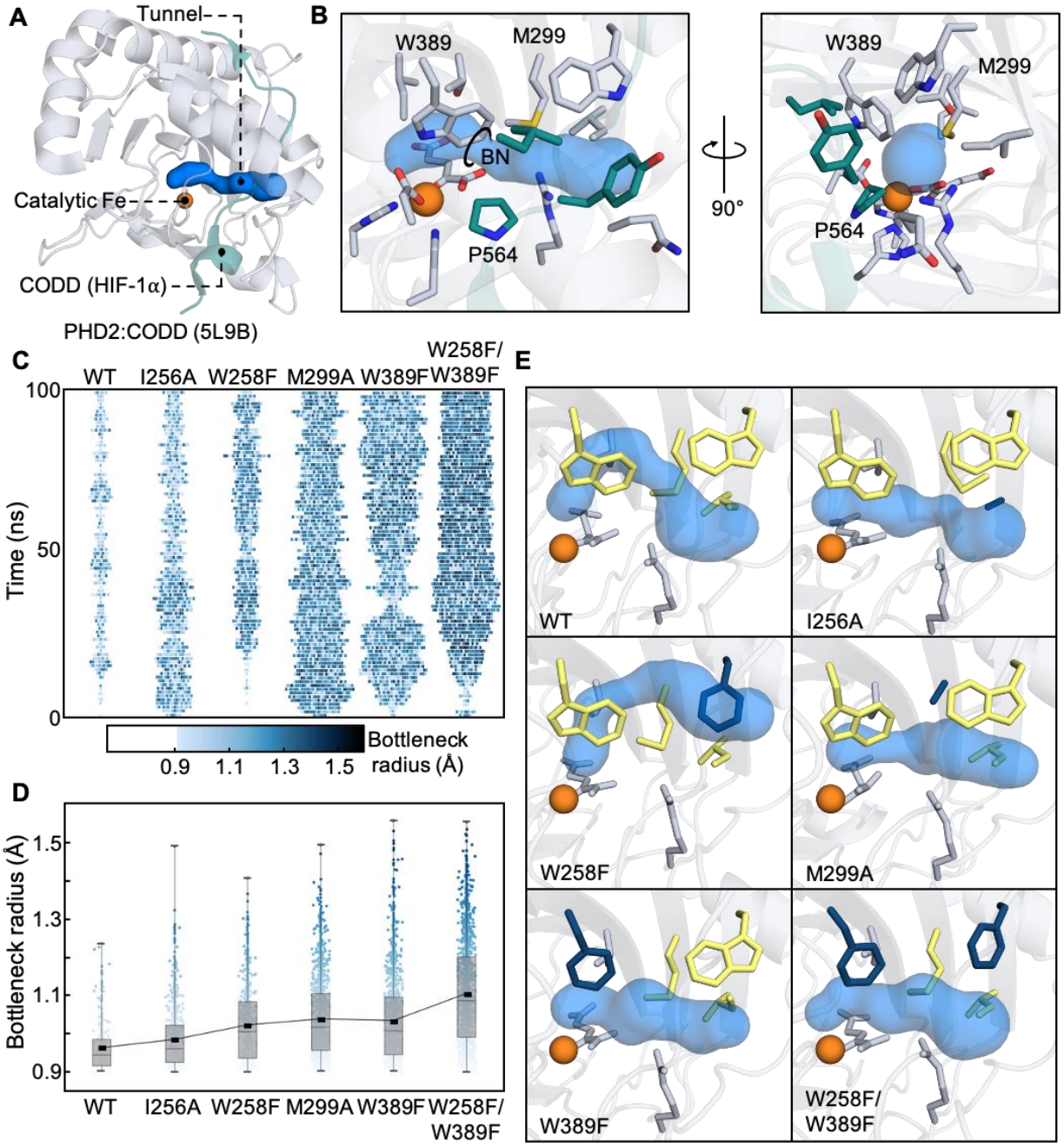

Figure 2. Engineering gas tunnel of PHD2. A) Full-view and **B)** zoomed-in crystal structure of PHD2:CODD (PDB: 5L9B) with CAVER computed O_2 tunnel. Tunnel is shown in blue, lining residues from PHD2 and CODD are shown in gray and teal, respectively. Bottleneck of the tunnel is represented as a circle labelled BN. **C)** Heat map depicting the frequency and bottleneck radius of the primary tunnel in PHD2 variants from three concatenated 100 ns MD trajectories. The width of lane gives a time-localized estimate of the duration for which the primary tunnel stays open and the color of each block represents the bottleneck radius of each observed tunnel. **D)** Impact of mutations on bottleneck radius (BR) from three concatenated 100 ns MD trajectories. Box plot reveals BR distribution (0, 25, 50, 75 and 100% quantile) for each variant. Trend line connects the average BR across PHD2 variants. **E)** Representative structures of MD simulated PHD2 variants showing the CAVER calculated tunnel in blue. WT tunnel forming residues that were targets of our protein design strategy are shown in yellow. Residues that were mutated to generate the specific variant shown in each panel are in dark blue. Residues that potentially constricted the tunnel but were not targets of design are shown in gray.

approach which involved mutating residues within PHD2's gas tunnel and investigating its impact on tunnel dynamics and constriction topology.

Target residues for our rational design study were selected by assessing multiple criteria such as positioning and orientation of the gas tunnel lining residues, their propensity to obstruct access to the iron core and their conservation in 1844 homologous PHD2 sequences. To begin with, we selected W258 and W389 for our studies as tryptophan has been previously shown to function as gates within tunnels to regulate substrate access and enzyme activity.[36,40,41,42] W258 is positioned at the entrance to the tunnel, and W389 is positioned directly in front of the iron center which makes these residues potential entry/exit gates for the O_2 gas. Additionally, both residues are highly conserved among PHD2s (**Fig. S2A,C**) indicating that they may contribute to tuning PHD2's O_2 sensing capability. We also selected M299 as a target residue for mutagenesis due to its role in forming the bottleneck with W389. Methionine is the most conserved amino acid at the 299 position, but other large amino acids such as histidine and glutamine are also observed in other PHD2s (**Fig. S2B**). We selected I256 as the fourth residue for rational design studies as it partially obstructs the tunnel entrance along with W258 and is mostly conserved among PHD2s (**Fig. S2A**). R252 was not considered as a target residue as it forms a salt bridge with D254 which has been shown to be crucial for CODD binding and hydroxylation activity of PHD2.[43] Lastly, T387 was also excluded as it forms an H-bond with iron's aqua ligand and mutations to this residue can change the modality of O_2 binding to iron.[33]

Next, we subjected WT PHD2 and mutants of target residues (I256A, W258A, W258F, M299A, W389A, and W389F) to molecular dynamics (MD) simulations to investigate how these mutations would affect protein structure and tunnel dynamics. MD simulations of W258A and W389A PHD2 variants demonstrated significantly altered placement of the CODD peptide and were excluded from further analysis (**Fig. S3-4)**. Instead, we included W258F/W389F PHD2 variant that replaces both bulky tryptophan residues in the tunnel with smaller phenylalanine in subsequent investigations. MD trajectories of WT and selected variants were analyzed using

Table 1. Gas tunnel statistics of WT and engineered PHD2 variants

Variant	% of frames with primary tunnel (Avg.) ± SD (%)	Avg. BR ± AD (Å)	Avg. Length ± AD (Å)	Avg. Curvature ± AD (Å)
WT	11.9 ± 12.1	0.95 ± 0.05	19 ± 4	1.5 ± 0.3
I256A	30.1 ± 2.6	0.98 ± 0.08	18 ± 2	1.4 ± 0.2
W258F	23.7 ± 10.2	0.97 ± 0.07	17 ± 3	1.4 ± 0.2
M299A	57.9 ± 19.0	1.0 ± 0.1	17 ± 2	1.3 ± 0.1
W389F	60.5 ± 14.8	1.0 ± 0.1	15 ± 2	1.2 ± 0.2
W258F/W389F	76.2 ± 9.0	1.1 ± 0.1	15 ± 2	1.2 ± 0.1

CAVER to understand how individual mutations affect the constriction topology and dynamics of the highest-ranked tunnel. We note that this highest-ranked tunnel is also the one identified in the crystal structure and will henceforth be referred to as the primary tunnel. Some lower-ranked tunnels were observed as well, but they were present minimally leading us to conclude that they did not contribute significantly to O_2 transport. To visualize how mutations could impact O_2 transport, we tracked the presence of the primary tunnel within three concatenated 100 ns MD trajectories (3000 total frames) for each PHD2 variant (**Fig. 2C**). Each data point in the plot indicates that the tunnel was found to be present in the corresponding MD frame or open for O_2 transport at that instant, and its color corresponds to its bottleneck radius. Absence of the primary tunnel in any MD frame leads to an absent data point and corresponds to the primary tunnel being closed for transport at that instant. We binned all data points into 1 ns interval along the time axis such that points corresponding to an open tunnel within that 1 ns interval are spread out horizontally. Such a representation eliminates overlapping points that could arise from limited resolution of the plot in the vertical direction. At the same time, the horizontal width of each lane gives a time-localized estimate of the duration for which the primary tunnel stays open as the simulation progresses. We also computed tunnel statistics for parameters such as the percentage of the total frames showing the primary tunnel, their bottleneck radius (BR), length, and curvature to quantify how the mutations affected the tunnel (**Table 1**). It is easy to see that the first lane (**Fig. 2C**) corresponding to WT PHD2 is characterized by a low density of points and is narrow in

width indicating that the tunnel is mostly closed and opens intermittently for short durations to severely limit O_2 transport. Furthermore, the tunnel when present in WT PHD2 possesses tight bottlenecks (avg. BR of 0.95 ± 0.05 Å, **Fig. 2D**). The next two lanes (**Fig. 2C-D**) for I256A and W258F mutants reveal higher point densities and sample wider bottlenecks suggesting potential for improved O_2 transportation. The last three lanes (**Fig. 2C-D**) corresponding to M299A, W389F and W258F/W389F variants reveal tunnels that stay mostly open (present in 58 ± 19%, 61 ± 15% and 76 ± 9% of simulation frames, respectively) and sample tunnel topologies with the widest bottlenecks. To gain structural insights into these observations, we compare the primary tunnel calculated by CAVER using a representative MD frame from each PHD2 variant. Beginning with the MD-simulated WT PHD2, we observe that its gas tunnel (top left panel, **Fig. 2E**) takes a rather curved path to the iron core as compared to the tunnel calculated from the crystal structure (**Fig. 2B**). In the majority of MD frames that contain this gas tunnel, the bottleneck is formed by M299 and 2OG with either R252 or W389. Mutation of I256 to Ala in the I256A variant creates space for bulky M299 to take an alternate conformation (top right panel, **Fig. 2E**) such that the methionine is no longer the bottleneck residue and affords a higher propensity for the tunnel to stay open. Mutating W258 to Phe in the W258F variant modifies the tunnel path at the entry location (middle left panel, **Fig. 2E**) such that O_2 can take a shorter and less curved path to the iron center. In the M299A variant, the 299 residue is no longer a bottle neck and O_2 can take a direct path to the iron-center (middle left panel, **Fig. 2E)**. In the W389F and the W258F/W389F variants, the constriction between the 299 and 389 residues are significantly relaxed allowing the tunnel to remain open and offers O_2 the shortest path to the iron-center (bottom panels, **Fig. 2E)**. Overall, our computational protein design studies reveal that it is possible to modify gas tunnel architecture with features that can enhance O_2 transport to the PHD2 active site.

To experimentally probe the impact of selected mutations to residues lining PHD2's gas tunnel on its biochemical activity, we expressed and purified WT PHD2 and its I256A, W258F,

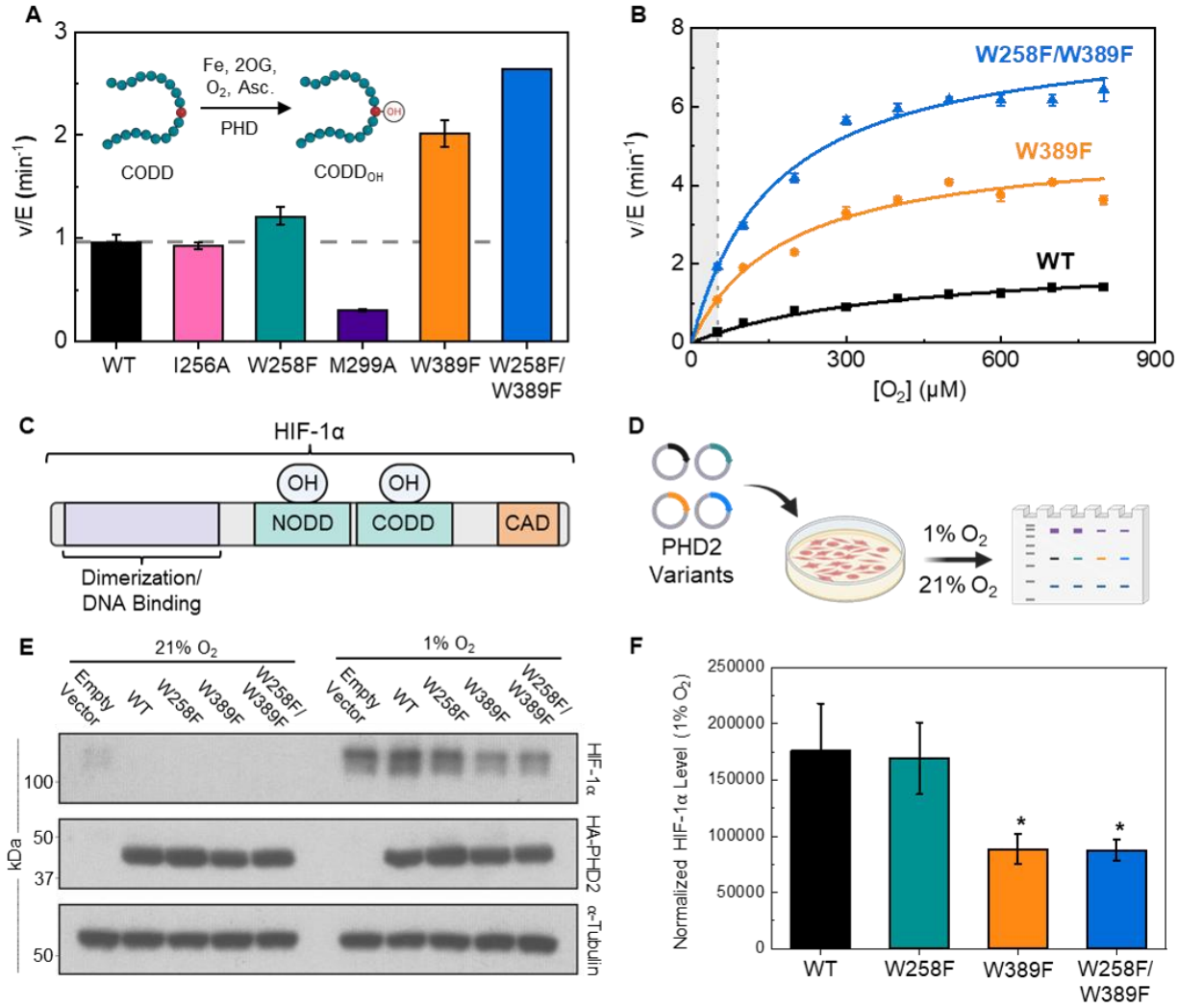

Figure 3. Gas tunnel engineered PHD2 variants display enhanced hydroxylation activity and reprogram HIF signaling in cells A) Average hydroxylation rate of CODD for PHD variants at atmospheric oxygen levels (21% or 256 μM O_2). Hydroxylation activity was determined by monitoring the conversion of CODD to $CODD_{OH}$ via MALDI-TOF MS. Averages and S.D. are from three independent experiments. **B)** Steady-state kinetics as a function of varied O_2 concentrations for PHD variants. Shaded gray area represents hypoxic oxygen concentrations (0-50 μM). Averages and S.D. for each data point are from two independent experiments. **C)** Schematic representation of various domains in the protein sequence of HIF-1α **D)** Schematic representation of the methodology of our cellular experiments. HEK-293T cells were transfected with plasmids expressing WT and PHD2 variants and incubated under normoxia (21% O_2) and extreme hypoxia (1% O_2). HIF-1α levels were determined using Western blot. **E)** Representative blots from our cellular studies. Under normoxia, PHD2 variant transfected cells showed complete degradation of HIF-1α. Under extreme hypoxia, WT and W258F transfected cells showed similar levels of HIF-1α, whereas W389F and W258F/W389F transfected cells showed a reduction of HIF-1α. **F)** Quantification of HIF-1α protein levels from Western blot. W389F and W258F/W389F transfected cells exhibit 50% less HIF-1α compared to wild-type (*$p < 0.05$). Values were quantified in ImageJ and normalized by WT PHD2 using the equation: *normalized HIF-1α = HIF-1α*(PHD2 variant/WT PHD2)*. Averages and S.D. are from three independent experiments.

M299A, W389F and W258F/W389F variants (**Fig. S5**). We also characterized the overall protein fold and stability of these PHD2 variants using Circular Dichroism (CD) and Thermal shift assays (TSA) (**Fig. S6 and S7**, respectively). CD studies showed that the designed variants resembled WT PHD2 in their overall secondary structure. At the same time, TSA data showed that the variants, albeit showing lower melting temperatures than WT, were quite stable at room temperature where our assays were performed at. Next, we assessed the hydroxylation activity of WT PHD2 and designed variants by monitoring the rate of conversion of the CODD peptide to the $CODD_{OH}$ peptide using mass spectrometry (**Fig. S8**).[44] Under atmospheric O_2 levels (256 μM or 21% O_2), WT PHD2 exhibits a CODD hydroxylation rate of 0.96 ± 0.075 min^{-1} (**Fig. 3A**). While I256A PHD2 displayed a tunnel with slightly improved access in the simulation, the mutant exhibits hydroxylation activity very similar to WT. The W258F variant, on the other hand, shows a notable 1.25-fold increase in hydroxylation catalysis further supporting W258's role as a tryptophan gate obstructing the O_2 gas tunnel at its entrance. Despite significantly enhanced gas tunnel characteristics in simulations of the M299A PHD2 variant, this mutant exhibited a 3-fold reduced activity. This result indicates that the Met299 residue plays an important role in hydroxylation catalysis beyond simply controlling/limiting O_2 access. Mutation of the W389 residue to phenylalanine in the W389F variant reveals a 2-fold enhancement in hydroxylation catalysis rate further affirming that the bottleneck forming W389 residue could be the major tryptophan gate in PHD2's gas tunnel. Ultimately, tandem mutations to both tryptophan gates in the W258F/W389F variant lead to the highest 2.5-fold enhancement in hydroxylation rate suggesting that these bulky residues act in tandem to restrict O_2 transport to the active site of PHD2. To verify that these tryptophan gates exert control on PHD2's hydroxylation catalysis through an O_2 dependent pathway, we conducted steady-state kinetic studies of CODD hydroxylation at varying O_2 concentrations for WT PHD2 and the highest activity variants, W389F and W258F/W389F. Fitting the data to the Michaelis-Menten model, we calculate a $K_{M(O2)}$ of 415 ± 36 μM, a catalytic first-order rate constant (k_{cat}) of 2.2 ± 0.1 min^{-1}, and catalytic efficiency

Table 2. Oxygen dependent kinetic constants of WT and tunnel engineered PHD2 variants

Variant	$K_M(O_2)$ (μM)	k_{cat} (min^{-1})	k_{cat}/K_M ($mM^{-1} \cdot min^{-1}$)
WT	415 ± 36	2.2 ± 0.1	5.3 ± 0.1
W389F	183 ± 16	5.1 ± 0.3	28.0 ± 0.1
W258F/W389F	161 ± 17	8.0 ± 0.3	58.5 ± 0.3

($k_{cat}/K_{M(O2)}$) of 5.3 ± 0.1 mM^{-1} min^{-1} for WT PHD2 (black curve, **Fig. 3B**) which matches previously reported[6] values (**Table 2, Fig. S9**). The W389F PHD2 variant reveals a 2.5-fold reduced $K_{M(O2)}$ (183 ± 16 μM) and a 2-fold enhanced k_{cat} (5.1 ± 0.3 min^{-1}) yielding a 5-fold enhancement in catalytic efficiency (28.0 ± 0.1 mM^{-1} min^{-1}) relative to WT PHD2. While the $K_{M(O2)}$ of the W258F/W389F PHD2 variant (161 ± 17 μM) is comparable to the W389F PHD2 variant, it has a 3.6-fold enhanced k_{cat} (8.0 ± 0.3 min^{-1}) compared to WT PHD2. Overall, W258F/W389F PHD2 exhibited an 11-fold higher $k_{cat}/K_{M(O2)}$ as compared to WT PHD2 suggesting that engineering of PHD2's gas tunnel can indeed enhance its HIF-1α hydroxylation performance.

Under hypoxia, tunnel engineered PHD2 variants exhibited up to 9-fold higher hydroxylation rates for HIF-1α CODD as compared to WT PHD2 (gray region in **Fig. 3B**). These results encouraged us to investigate the impact of designed PHD2 variants on cellular HIF-1α levels under hypoxic conditions. PHD2 senses the presence of O_2 in cells by catalyzing hydroxylation of HIF-1α (**Fig. 3C**), which primes the latter for proteasomal degradation. The relatively low O_2 levels under hypoxia inhibits PHD2 resulting in cellular accumulation of HIF-1α. To investigate if designed PHD2 variants modulate cellular HIF-1α levels, we transfected HEK-293T cells with plasmids expressing WT, W258F, W389F, and W258F/W389F PHD2 variants and incubated them under atmospheric O_2 levels (21% O_2) and extreme hypoxic (1% O_2) conditions (**Fig. 3D**). We used western blot to monitor intracellular HIF-1α and PHD2 levels with α-tubulin as the loading control. At 21% O_2, cells transfected with empty vector displayed minor HIF-1α levels while cells transfected with WT and PHD2 variants exhibited undetectable HIF-1α (representative blots in **Fig. 3E**) suggesting that PHD2 expressed via exogenous vector can

facilitate hydroxylation and proteasomal degradation of HIF-1α. Incubation under extreme hypoxia (1% O_2) allowed for HIF-1α accumulation in cells, so any differences in HIF-1α levels between WT PHD2 and engineered variants could be quantified. HIF-1α levels were normalized against a ratio of PHD2 variant to WT PHD2 to ensure that varying levels of transfection did not skew quantification. While W258F PHD2 exhibited higher hydroxylation activity with HIF-1α CODD mimic as compared to WT PHD2*, in cellulo* this mutant displayed HIF-1α levels similar to WT PHD2 (**Fig 3F**). The W258F mutation in PHD2 along with opening its gas tunnel potentially also modulates hydrophobic contacts with CODD domain (teal curve, **Fig. S4**). Such modulation could perturb protein-protein interaction (PPI) between full-length HIF-1α and W258F PHD2 cancelling out any tunnel-based enhancement effects on W258F PHD2's cellular activity. In contrast, W389F mutant alone or when combined with W258F in W258F/W389F PHD2 variant demonstrates a 2-fold decrease in HIF-1α levels. Overall, these cellular studies along with our computational modeling and biochemical studies confirm the role of W389 as an important regulatory gate for transporting O_2 to PHD2's iron core. These results also demonstrate the potential of using gas tunnel engineered or activated PHD2 variants to deceive cellular HIF signaling pathways, such that cells display physoxia-like HIF-1α levels[45] even under extreme hypoxia (1% O_2).

Conclusion

Although biocatalysts play important roles in physiology, their engineered forms have not yet been used to modulate cellular function. This is due to several challenges, including: (1) the efficient delivery of the biocatalyst to the cell; (2) the provision of all the required co-substrates to the engineered enzyme; and (3) ensuring that the engineered biocatalyst retains its required PPI in the cell. Our studies with PHD2 as a model system shows that these challenges can be overcome. First, we show that engineered PHD2 mutants can be delivered to HEK-293T cells as plasmids that express the biocatalyst at levels comparable to WT. They utilize the same cofactors as WT PHD2 which are abundant in cells (e.g., iron and 2OG) and alternative strategies for providing co-substrates are not needed. Lastly, by using a PHD2 structure that mimics its interaction with the

HIF-1α partner protein for our computationally guided enzyme engineering study and by only selecting mutations that do not disrupt the PPI with HIF-1α in MD simulations, we have been able to engineer PHD2 mutants that enhance HIF-1α hydroxylation and degradation in human kidney cells. We note that hypoxia-induced HIF-1α is accumulated in various disease types, including cancer and Alzheimer's and numerous small-molecule and gene-editing methodologies that target HIF-1α have been developed, some of which are currently in clinical trials.[46,47] While downstream inhibition of HIF signaling pathways are being aggressively pursued, we have achieved the same by activating PHD2, a biocatalyst that is upstream to the transcription factor. In all, our work represents a new modality in which we activate enzymatic sensors upstream to the transcription factor as compared to conventional strategies of inhibiting downstream signaling cascades. Beyond presenting a novel application of engineered biocatalysts, our studies also represent a systematic investigation into how gas tunnel architectures in PHD2-like enzymatic sensors can control O_2 sensing capability. It also highlights the potential of gas-tunnel engineering as a pathway to tune O_2 sensing capability and cellular function of other iron-based enzymatic sensors such as PHD1, PHD3, AspH and FIH. Overall, this work elucidates how non-heme iron proteins utilize gas tunnels to optimize their O_2 sensing capability to match physiological needs as well as presents a novel application of engineered biocatalysts in the realm of cellular biology and hypoxia signaling.

Methods

Materials: All chemicals were purchased from commercial vendors. All primers were purchased from Integrated DNA Technologies (Coralville, IA, USA). The sequence of the peptide substrate (CODD) was DLDLEMLAPYIPMDDDFQL, and it was derived from native HIF-1α. CODD (99% purity) was synthesized and purchased from Peptide Synthesis Services (University of Minnesota, Internal Service Organization).

***Bioinformatic analysis*:** To observe sequence conservation at the 256, 258, 299, and 389 residue positions of PHD2, the PHD2 amino acid sequence ($PHD2_{1-426}$) was BLAST searched in the non-redundant protein database. An E-value cutoff of e^{-9} produced 4,966 protein sequences. The sequences were filtered using CD-HIT to remove redundant sequences of 99% similarity.[48] The sequences were further filtered to remove sequences that contained more than 550 amino acids or less than 300 amino acids to ensure the sequences had similar sequence length to PHD2 (426 amino acids). This produced 1844 sequences for the final alignment. The sequences were aligned using the MAFFT alignment algorithm. Alignment results were viewed in AliView, and logos plots were created in WebLogo.[49,50] Phylogenetic trees were constructed in the MEGA 11 software using the neighbor joining method (1000 replicates).[51] Sequences were clustered in groups of 10 to ensure adequate visualization of tree anatomy.

***Tunnel analysis of PHD2 crystal structure*:** CAVER Analyst 2 was used to identify possible O_2 pathways in the WT PHD2:CODD crystal structure (PDB: 5L9B).[52,38] The catalytic iron atom was used as the starting point with a maximum starting distance of 3 Å and a desired radius of 5 Å. The minimum probe radius was set to 0.9 with a shell depth of 4 and a shell radius of 3. The tunnel clustering threshold was set to 3.5.

***Molecular dynamics of PHD2 variants*:** Molecular dynamics simulations were used to determine how amino acid mutations affected the proposed tunnels of PHD2 and its variants The starting structure of WT PHD2 bound to CODD was taken from the Protein Data Bank (PDB: 5L9B) and mutations were induced using UCSF Chimera.[38,53] Parameters for the PHD iron-center were determined using the *MCPB.py* module of Amber16.[54] Explicit hydrogen atoms were added to the protein and its mutant structures using the *tleap* module of Amber16. Proteins were solvated in a truncated octahedron unit cell with TIP3P water molecules (neutralized with Na^+ ions) with a 12.0 Å solvent buffer between the protein and the closest edge of the unit cell.[55] The system was simulated with the Amber ff14SB forcefield. The GPU-accelerated *pmemd* code of Amber16 was used to perform all steps of molecular dynamics (MD).[56] The system was minimized using a

seven-step process consisting of 1000 steps of steepest descent minimization followed by 5000 steps of conjugate gradient minimization for each step. For the first step of minimization, all solute heavy atoms were subjected to restraints starting at 10.0 kcal/mol/Å^2. Restraints were lowered systematically over the course of each step with the last step having a restraint of 0.0 kcal/mol/Å^2. Next, the system was heated linearly from 10.0 K to 298.0 K over 2.0 ns. During heating, all solute atoms were subjected to a restraint of 10.0 kcal/mol/Å^2. A maximum temperature of 298.0 K was chosen in an effort to mimic the conditions at which the experimental trials were completed. Equilibration of the system was carried out over 3.5 ns at a constant temperature of 298.0 K. All solute heavy atoms were subjected to restraints of 10.0 kcal/mol/Å^2 for the first 0.5 ns, and restraints were decreased geometrically every 0.5 ns until reaching a restraint weight of 0.0 kcal/mol/Å^2 for the final 0.5 ns. After equilibration of the system, unrestrained MD was performed at a constant pressure of 1 atm and constant temperature of 298.0 K. The coordinates were saved every 100 ps, and all systems were simulated without restraints for 100 ns in triplicate. Minimization, heating, equilibration, and unrestrained MD is in accordance with previously published works.[57,58] MD analysis (RMSD, b-factor, and distance) was performed using the *cpptraj* module of Amber16.[59] The resulting values for each simulation were averaged for each PHD2 variant and reported. The visualization of the completed trajectories was carried out using PyMOL and UCSF Chimera.[53,60]

***Tunnel analysis of molecular dynamics trajectories*:** CAVER Analyst 2 was used to identify possible O_2 pathways in the in the molecular dynamics trajectories of PHD2 variants. Each of the triplicate 100 ns trajectories (1000 frames) for each PHD variant (6 variants) were analyzed in this way (18,000 total frames). The catalytic iron atom was used as the starting point with a maximum starting distance of 3 Å and a desired radius of 5 Å. The minimum probe radius was set to 0.9 with a shell depth of 4 and a shell radius of 3. The tunnel clustering threshold was set to 3.5. The tunnel parameters (occupancy, average bottleneck radius, maximum bottleneck radius, length, and curvature) for each simulation were averaged for each PHD2 variant and reported.

Site-directed mutagenesis: Site-directed mutagenesis was used to create point mutations in PHD2. For recombinant protein expression, $PHD2_{181-426}$ (wild-type and mutants) was incorporated into pET-28a(+) expression vector with an N-terminal His_6 tag. Site-directed mutagenesis was performed on the wild-type PHD plasmid to create I256A, W258F, M299A, W389F, and W258F/W389F mutations using Phusion site-directed mutagenesis kit (Thermofisher Scientific). The primers (5' → 3') for site-directed mutagenesis were: I256A (forward – GAGGCGATAAGGCCACCTGGATCGA, reverse – GGATGTCCTTGGACGAGTCACTCTTC), W258F (forward – GATAAGAT CACCTTCATCGAGGGCAAG, reverse – GCCTCGGATGTCCTTGGACGAGT), M299A (forward – CGGACGAAAGCCGCGGTTGCTTGTTAT, reverse – GCCATTGATTT TGTAGCTGCCCAGCT), W389F (forward – CGCAATAACTGTTTTCTATTTTGATGCAGA, reverse – TACCTTGTAGCATATGCTG GTTGTACTTC). PCR was executed using a standard two-step protocol. Presence of mutations were confirmed using classic Sanger sequencing at University of Minnesota Genomics Center (UMGC). T7 promoter (TAATACGACTCACTATAGGG) and T7 terminator (GCTAGTTATTGCTCAGCGG) were used for sequencing.

For cell transfection, $PHD2_{1-426}$ (wild-type and mutants) was incorporated into a prk5-HA expression vector. Site-directed mutagenesis was performed on the wild-type PHD2 plasmid to create I256A, W258F, M299A, W389F, and W258F/W389F mutations using Phusion site-directed mutagenesis kit (Thermofisher Scientific). The primers for site-directed mutagenesis were the same as previously mentioned. PCR was executed using a standard two-step protocol. Presence of mutations were confirmed using Nanopore sequencing at Plasmidsaurus.

Protein expression: BL-21(DE3) E. coli (Thermofisher Scientific) were transformed with pET-28a(+) expression vector containing His6-$PHD_{181-426}$ (wild-type and mutants). Cells were grown in 2XYT media supplemented with kanamycin (50 µg/mL) at 37 °C and 220 RPM to an OD_{600} of 0.65. Protein expression was induced with 0.5 mM IPTG at 18 °C and 220 RPM for 18 hours. Cells were harvested by centrifugation and stored at -20 °C until purification.

***Protein purification*:** Cells were resuspended in buffer (20 mM Tris HCl, 500 mM NaCl, and 5 mM imidazole at pH = 7.5) with Pierce Protease Inhibitor Tablets (Thermofisher Scientific) until homogenous. Cells were lysed through sonification followed by centrifugation and filtration. Cell lysate was purified using Ni-NTA affinity column (Cytiva) with running buffer (20 mM Tris HCl, 500 mM NaCl, and 5 mM imidazole at pH = 7.5) and elution buffer (20 mM Tris HCl, 100 mM NaCl, and 300 mM imidazole at pH = 7.5). Further purification was performed using a size-exclusion column (HiLoad Superdex 75pg 26/600, Cytiva). Protein purities were assessed using SDS-PAGE and concentrations were determined using UV-Vis spectroscopy. All protein purities were assessed at > 95% via ImageJ. Protein was exchanged into storage buffer (50 mM Tris HCl, 5% glycerol, pH = 7.5) and stored at 15 mg/mL at -80 °C.

***Thermal shift assays*:** To assess the thermostability of PHD2 variants, thermal shift assays were performed. Assays were carried out in a MyiQ2 rt-PCR detection system (Bio-Rad). Protein unfolding was monitored with SYPRO orange (Thermofisher Scientific) using a default FAM excitation and emission protocol. Each well contained 4 µM protein, 1 mM $(NH_4)_2Fe(SO_4)_2$, 1 mM 2OG, and 5x SYPRO orange in 50 mM Tris (pH = 7.5) with a final volume of 40 µL. The temperature was linearly increased by 0.5 °C every 30 seconds with fluorescence readings being taken every 30 seconds. Melting temperatures (T_m) were determined by taking the negative first derivative of the raw fluorescence data and finding the global minimum value.

Circular dichroism: Circular dichroism (CD) was used to assess the secondary structure of PHD2 variants. Spectra were obtained on a J-815 CD spectropolarimeter (JASCO) using 1 mm cuvette. Data was acquired with a 50 nm/min scan rate, 2 sec D.I.T., 2 nm bandwidth, and 1 nm data pitch. Data was acquired continuously from 255 nm to 195 nm in triplicate for each variant. The HT voltage was maintained below 700 V for the entirety of each scan. Protein was prepared at 5 µM in 10 mM phosphate buffer (pH = 7.5). Raw data was converted to molar ellipticity to correct for protein concentration differences.

***Assessment of hydroxylation activity of PHD2 variants at atmospheric oxygen levels*:** Initial hydroxylation activity of PHD2 variants was assessed by monitoring hydroxylation activity at atmospheric oxygen levels. Reactions were carried out at conditions of 50 µM $(NH_4)_2Fe(SO_4)_2$, 100 µM CODD peptide, 300 µM 2OG, and 4 mM sodium ascorbate in 50 mM Tris buffer (pH = 7.5) at 20 °C in a 1.7 mL reaction tube. MALDI-TOF mass spectrometry was used to monitor the conversion of CODD [(M + Na^+), 2276 m/z calculated, 2276 m/z observed] to $CODD_{OH}$ [(M + O + Na^+), 2292 m/z calculated, 2292 m/z observed]. Reactions were quenched at different time points by spotting 1 µL of reaction mix directly on to the MALDI target plate with 1 µL of saturated 4-α-cyanohydroxycinnamic acid dissolved in 50% acetonitrile and 0.1% trifluoroacetic acid. Spots were analyzed using a positive reflectron method in a Daltonics Autoflex Speed MALDI-TOF mass spectrometer (Bruker). Percent conversion to $CODD_{OH}$ was calculated by comparing the relative intensities of the CODD and $CODD_{OH}$ species.

***Steady-state kinetics assays*:** Steady-state constants for PHD2 variants were obtained by monitoring hydroxylation activity at saturating concentrations of 10 µM $(NH_4)_2Fe(SO_4)_2$, 100 µM CODD peptide, 300 µM 2OG, and 2 mM sodium ascorbate in 50 mM Tris (pH = 7.5) at 25 °C. Reaction was performed in an Oxytherm instrument (Hansatech) with a Clark electrode to monitor oxygen concentration. Concentration of dissolved oxygen was controlled by mixing varying ratios of N_2 purged buffer and O_2 purged buffer and equilibrating in the Oxytherm reaction vessel. MALDI-TOF mass spectrometry was used to monitor the conversion of CODD [(M + Na^+), 2276 m/z calculated, 2276 m/z observed] to $CODD_{OH}$ [(M + O + Na^+), 2292 m/z calculated, 2292 m/z observed]. Reactions were quenched at different time points by spotting 1 µL of reaction mix directly on to the MALDI target plate with 1 µL of saturated 4-α-cyanohydroxycinnamic acid dissolved in 50% acetonitrile and 0.1% trifluoroacetic acid. Spots were analyzed using a positive reflectron method in a Daltonics Autoflex Speed MALDI-TOF mass spectrometer (Bruker).[44] Percent conversion to $CODD_{OH}$ was calculated by comparing the relative intensities of the CODD

and $CODD_{OH}$ species. Methionine oxidation (~6%) was subtracted, and the data were fitted with the Michaelis-Menten equation.

***Mammalian cell culture and plasmid transfection*:** HEK293T were cultured in Dulbecco's Modified Eagle's medium (DMEM) (11965092, Gibco) supplemented with 10% Fetal Bovine Serum (F0926, Sigma) and 1% penicillin-streptomycin (Corning). The cells were maintained in a 37 °C incubator supplied with 5% CO_2. For plasmid transient transfections, cells were seeded 24 hours before transfection at a density of 1×10^5 cells/ml, then transfected with 0.2 μg plasmid for the next 24 hours. For hypoxia treatment, 24 hours after transfection, cells were cultured in a hypoxia chamber (BioSperix) in the regular 37 °C incubator supplied with 1% O_2/5% CO_2/94% N_2 for 24 hours. Cell lines were regularly tested for mycoplasma (G238, abm) and found to be negative.

***Cell lysis and Western blotting*:** Cells were harvested by washing with cold PBS and lysed in cell lysis buffer (150 mM NaCl, 0.5% NP-40, 50 mM Tris-HCL, 10% glycerol, 1% SDS, pH 7.5, supplemented with 1x protease inhibitor cocktail (Roche)) on ice. The extracted proteins were separated in homemade SDS-PAGE gel and transferred onto PVDF membrane. Blocking was done with 5% skim milk (BD) in TBST (TBS+0.1% Tween-20). After blocking, the membrane was incubated with primary antibody overnight at 4°C and washed with TBST for 3 times, then incubated with HRP-linked secondary antibody (Cell Signaling Technology, #7074 and #7076) for 1 hour and washed with TBST. The signal was developed with Luminata Crescendo Western HRP Substrate (WBLUR0500, Millipore) and captured on X-ray film. Primary antibodies used in the current study included Anti-HA (660002, Biolegend), HIF1α (SAB2702132, Millipore), α-Tubulin (T6199, Sigma). Protein bands were quantified using ImageJ.

Acknowledgements: Bhagi-Damodaran Lab acknowledges funds from Regents of the University of Minnesota, American Cancer Society and RCSA Cottrell Foundation for supporting this

research. Chen lab acknowledge their funding resources NIH Grant (R35GM124896) and NSF Grant CHE-1753154.

Author Contributions: PW performed all computational, biochemical and biophysical studies and analysis. HO performed cellular studies and analysis. JDC helped with expressing, purifying and performing biochemical assay with I256A PHD2 variant. ARD, YC, and ABD supervised the study. PW, ARD, and ABD wrote the manuscript with inputs from all authors.

References

1. Duewel, S. *et al.* Directed Evolution of an Fe^{II} -Dependent Halogenase for Asymmetric C(sp^3)–H Chlorination. *ACS Catal.* **10**, 1272–1277 (2020).
2. Xiao, X. *et al.* Tackling the Challenges of Enzymatic (Bio)Fuel Cells. *Chem. Rev.* **119**, 9509–9558 (2019).
3. Outten, F. W. & Theil, E. C. Iron-Based Redox Switches in Biology. *Antioxid. Redox Signal.* **11**, 1029–1046 (2009).
4. Simpson, R. J. & McKie, A. T. Iron and oxygen sensing: a tale of 2 interacting elements? *Metallomics* **7**, 223–231 (2015).
5. Damodaran, A. R. & Bhagi-Damodaran, A. Integrating UV-Vis Spectroscopy and Oxygen Optode for Accurate Determination of Oxygen Affinity of Proteins. in *Oxygen Sensing* (ed. Weinert, E. E.) vol. 2648 1–10 (Springer US, 2023).
6. Liu, T. *et al.* Biochemical and biophysical analyses of hypoxia sensing prolyl hydroxylases from Dictyostelium discoideum and Toxoplasma gondii. *J. Biol. Chem.* **295**, 16545–16561 (2020).

7. Smith, A. T. *et al.* Functional Divergence of Heme-Thiolate Proteins: A Classification Based on Spectroscopic Attributes. *Chem. Rev.* **115**, 2532–2558 (2015).

8. Olea, C., Boon, E. M., Pellicena, P., Kuriyan, J. & Marletta, M. A. Probing the Function of Heme Distortion in the H-NOX Family. *ACS Chem. Biol.* **3**, 703–710 (2008).

9. Schofield, C. J. & Ratcliffe, P. J. Oxygen sensing by HIF hydroxylases. *Nat. Rev. Mol. Cell Biol.* **5**, 343–354 (2004).

10. Bruick, R. K. & McKnight, S. L. A Conserved Family of Prolyl-4-Hydroxylases That Modify HIF. *Science* **294**, 1337–1340 (2001).

11. Epstein, A. C. R. *et al.* C. elegans EGL-9 and Mammalian Homologs Define a Family of Dioxygenases that Regulate HIF by Prolyl Hydroxylation. *Cell* **107**, 43–54 (2001).

12. Williams, M. T. *et al.* Metalloprotein enabled redox signal transduction in microbes. *Curr. Opin. Chem. Biol.* **76**, 102331 (2023).

13. Raven, E. L. A short history of heme dioxygenases: rise, fall and rise again. *JBIC J. Biol. Inorg. Chem.* **22**, 175–183 (2017).

14. Scotti, J. S. *et al.* Human oxygen sensing may have origins in prokaryotic elongation factor Tu prolyl-hydroxylation. *Proc. Natl. Acad. Sci.* **111**, 13331–13336 (2014).

15. Lippl, K. *et al.* Born to sense: biophysical analyses of the oxygen sensing prolyl hydroxylase from the simplest animal Trichoplax adhaerens. *Hypoxia* **Volume 6**, 57–71 (2018).

16. McDonough, M. A., Li, V., Flashman, E., Chowdhury, R. & Mohr, C. Cellular oxygen sensing: Crystal structure of hypoxia-inducible factor prolyl hydroxylase (PHD2).

17. Flagg, S. C., Giri, N., Pektas, S., Maroney, M. J. & Knapp, M. J. Inverse Solvent Isotope Effects Demonstrate Slow Aquo Release from Hypoxia Inducible Factor-Prolyl Hydroxylase (PHD2). *Biochemistry* **51**, 6654–6666 (2012).

18. Loenarz, C. *et al.* The hypoxia-inducible transcription factor pathway regulates oxygen sensing in the simplest animal, *Trichoplax adhaerens*. *EMBO Rep.* **12**, 63–70 (2011).

19. Arsenault, P. R., Song, D., Chung, Y. J., Khurana, T. S. & Lee, F. S. The Zinc Finger of Prolyl Hydroxylase Domain Protein 2 Is Essential for Efficient Hydroxylation of Hypoxia-Inducible Factor α. *Mol. Cell. Biol.* **36**, 2328–2343 (2016).

20. McKeown, S. R. Defining normoxia, physoxia and hypoxia in tumours—implications for treatment response. *Br. J. Radiol.* **87**, 20130676 (2014).

21. Xie, D., King, T. L., Banerjee, A., Kohli, V. & Que, E. L. Exploiting Copper Redox for ^{19}F Magnetic Resonance-Based Detection of Cellular Hypoxia. *J. Am. Chem. Soc.* **138**, 2937–2940 (2016).

22. He, W., Batty-Stuart, S., Lee, J. E. & Ohh, M. HIF-1α Hydroxyprolines Modulate Oxygen-Dependent Protein Stability Via Single VHL Interface With Comparable Effect on Ubiquitination Rate. *J. Mol. Biol.* **433**, 167244 (2021).

23. Flashman, E. *et al.* Kinetic Rationale for Selectivity toward N- and C-terminal Oxygen-dependent Degradation Domain Substrates Mediated by a Loop Region of Hypoxia-Inducible Factor Prolyl Hydroxylases. *J. Biol. Chem.* **283**, 3808–3815 (2008).

24. Min, J.-H. *et al.* Structure of an HIF-1α-pVHL Complex: Hydroxyproline Recognition in Signaling. *Science* **296**, 1886–1889 (2002).

25. Lisztwan, J., Imbert, G., Wirbelauer, C., Gstaiger, M. & Krek, W. The von Hippel-Lindau tumor suppressor protein is a component of an E3 ubiquitin-protein ligase activity. *Genes Dev.* **13**, 1822–1833 (1999).

26. Wood, S. M., Gleadle, J. M., Pugh, C. W., Hankinson, O. & Ratcliffe, P. J. The Role of the Aryl Hydrocarbon Receptor Nuclear Translocator (ARNT) in Hypoxic Induction of Gene Expression. *J. Biol. Chem.* **271**, 15117–15123 (1996).

27. Jiang, B.-H., Rue, E., Wang, G. L., Roe, R. & Semenza, G. L. Dimerization, DNA Binding, and Transactivation Properties of Hypoxia-inducible Factor 1. *J. Biol. Chem.* **271**, 17771–17778 (1996).

28. Wenger, R. H., Stiehl, D. P. & Camenisch, G. Integration of Oxygen Signaling at the Consensus HRE. *Sci. STKE* **2005**, (2005).

29. Semenza, G. L. HIF-1 mediates metabolic responses to intratumoral hypoxia and oncogenic mutations. *J. Clin. Invest.* **123**, 3664–3671 (2013).

30. Muz, B., de la Puente, P., Azab, F. & Azab, A. K. The role of hypoxia in cancer progression, angiogenesis, metastasis, and resistance to therapy. *Hypoxia* 83 (2015) doi:10.2147/HP.S93413.

31. Sun, X. *et al.* Hypoxia facilitates Alzheimer's disease pathogenesis by up-regulating *BACE1* gene expression. *Proc. Natl. Acad. Sci.* **103**, 18727–18732 (2006).

32. March-Diaz, R. *et al.* Hypoxia compromises the mitochondrial metabolism of Alzheimer's disease microglia via HIF1. *Nat. Aging* **1**, 385–399 (2021).

33. Pektas, S., Taabazuing, C. Y. & Knapp, M. J. Increased Turnover at Limiting O_2 Concentrations by the Thr ^{387} → Ala Variant of HIF-Prolyl Hydroxylase PHD2. *Biochemistry* **54**, 2851–2857 (2015).

34. Domene, C., Jorgensen, C. & Schofield, C. J. Mechanism of Molecular Oxygen Diffusion in a Hypoxia-Sensing Prolyl Hydroxylase Using Multiscale Simulation. *J. Am. Chem. Soc.* **142**, 2253–2263 (2020).

35. Tilton, R. F., Kuntz, I. D. & Petsko, G. A. Cavities in proteins: structure of a metmyoglobin xenon complex solved to 1.9 .ANG. *Biochemistry* **23**, 2849–2857 (1984).

36. Winter, M. B., Herzik, M. A., Kuriyan, J. & Marletta, M. A. Tunnels modulate ligand flux in a heme nitric oxide/oxygen binding (H-NOX) domain. *Proc. Natl. Acad. Sci.* **108**, (2011).

37. Chovancova, E. *et al.* CAVER 3.0: A Tool for the Analysis of Transport Pathways in Dynamic Protein Structures. *PLoS Comput. Biol.* **8**, e1002708 (2012).

38. Chowdhury, R. *et al.* Structural basis for oxygen degradation domain selectivity of the HIF prolyl hydroxylases. *Nat. Commun.* **7**, 12673 (2016).

39. Tarhonskaya, H. *et al.* Investigating the contribution of the active site environment to the slow reaction of hypoxia-inducible factor prolyl hydroxylase domain 2 with oxygen. *Biochem. J.* **463**, 363–372 (2014).

40. Biedermannová, L. *et al.* A Single Mutation in a Tunnel to the Active Site Changes the Mechanism and Kinetics of Product Release in Haloalkane Dehalogenase LinB. *J. Biol. Chem.* **287**, 29062–29074 (2012).

41. Kim, S. M. *et al.* O2-tolerant CO dehydrogenase via tunnel redesign for the removal of CO from industrial flue gas. *Nat. Catal.* **5**, 807–817 (2022).

42. Jones, J. C., Banerjee, R., Shi, K., Aihara, H. & Lipscomb, J. D. Structural Studies of the *Methylosinus trichosporium* OB3b Soluble Methane Monooxygenase Hydroxylase and Regulatory Component Complex Reveal a Transient Substrate Tunnel. *Biochemistry* **59**, 2946–2961 (2020).

43. Chowdhury, R. *et al.* Structural Basis for Binding of Hypoxia-Inducible Factor to the Oxygen-Sensing Prolyl Hydroxylases. *Structure* **17**, 981–989 (2009).

44. Mingroni, M. A., Chaplin Momaney, V., Barlow, A. N., Jaen Maisonet, I. & Knapp, M. J. Measurement of kinetic isotope effects on peptide hydroxylation using MALDI-MS. in *Methods in Enzymology* vol. 679 363–380 (Elsevier, 2023).

45. Bracken, C. P. *et al.* Cell-specific Regulation of Hypoxia-inducible Factor (HIF)-1α and HIF-2α Stabilization and Transactivation in a Graded Oxygen Environment. *J. Biol. Chem.* **281**, 22575–22585 (2006).

46. Li, Z., You, Q. & Zhang, X. Small-Molecule Modulators of the Hypoxia-Inducible Factor Pathway: Development and Therapeutic Applications. *J. Med. Chem.* **62**, 5725–5749 (2019).

47. Li, M. *et al.* Knockdown of hypoxia-inducible factor-1 alpha by tumor targeted delivery of CRISPR/Cas9 system suppressed the metastasis of pancreatic cancer. *J. Controlled Release* **304**, 204–215 (2019).

48. Fu, L., Niu, B., Zhu, Z., Wu, S. & Li, W. CD-HIT: accelerated for clustering the next-generation sequencing data. *Bioinformatics* **28**, 3150–3152 (2012).

49. Larsson, A. AliView: a fast and lightweight alignment viewer and editor for large datasets. *Bioinformatics* **30**, 3276–3278 (2014).

50. Crooks, G. E., Hon, G., Chandonia, J.-M. & Brenner, S. E. WebLogo: A Sequence Logo Generator: Figure 1. *Genome Res.* **14**, 1188–1190 (2004).

51. Tamura, K., Stecher, G. & Kumar, S. MEGA11: Molecular Evolutionary Genetics Analysis Version 11. *Mol. Biol. Evol.* **38**, 3022–3027 (2021).

52. Jurcik, A. *et al.* CAVER Analyst 2.0: analysis and visualization of channels and tunnels in protein structures and molecular dynamics trajectories. *Bioinformatics* **34**, 3586–3588 (2018).

53. Pettersen, E. F. *et al.* UCSF Chimera?A visualization system for exploratory research and analysis. *J. Comput. Chem.* **25**, 1605–1612 (2004).

54. Li, P. & Merz, K. M. MCPB.py: A Python Based Metal Center Parameter Builder. *J. Chem. Inf. Model.* **56**, 599–604 (2016).

55. Jorgensen, W. L. & Madura, J. D. Quantum and statistical mechanical studies of liquids. 25. Solvation and conformation of methanol in water. *J. Am. Chem. Soc.* **105**, 1407–1413 (1983).

56. Salomon-Ferrer, R., Götz, A. W., Poole, D., Le Grand, S. & Walker, R. C. Routine Microsecond Molecular Dynamics Simulations with AMBER on GPUs. 2. Explicit Solvent Particle Mesh Ewald. *J. Chem. Theory Comput.* **9**, 3878–3888 (2013).

57. Prins, R., Windsor, P., Miller, B. R. & Maiden, S. Alleles of *unc-33* /CRMP exhibit defects during *Caenorhabditis elegans* epidermal morphogenesis. *Dev. Dyn.* **251**, 1741–1753 (2022).

58. Windsor, P. K. *et al.* Biflavonoid-Induced Disruption of Hydrogen Bonds Leads to Amyloid-β Disaggregation. *Int. J. Mol. Sci.* **22**, 2888 (2021).

59. Roe, D. R. & Cheatham, T. E. PTRAJ and CPPTRAJ: Software for Processing and Analysis of Molecular Dynamics Trajectory Data. *J. Chem. Theory Comput.* **9**, 3084–3095 (2013).

60. The PyMOL Molecular Graphics System, Version 2.0, Schrodinger, LLC.